GLONASS-R: GNSS reflectometry with an FDMA based satellite navigation system

T. Hobiger[1], R. Haas[2] and J. S. Löfgren[2]

Corresponding author: T. Hobiger, Applied Electromagnetic Research Institute, National

Institute of Information and Communications Technology, 4-2-1 Nukui-Kitamachi, Koganei,

184-8795 Tokyo, Japan. (hobiger@nict.go.jp)

[1]Applied Electromagnetic Research

Institute, National Institute of Information

and Communications Technology,Japan.

[2]Department of Earth and Space Sciences,

Chalmers University of Technology,

Gothenburg, Sweden

The information from reflected Global Navigation Satellite System (GNSS) signals can become a valuable data source, from which geophysical properties can be deduced. This approach, called GNSS-Reflectometry (GNSS-R), can be used to develop instruments that act like an altimeter when arrival times of direct and reflected signals are compared. Current GNSS-R systems usually entirely rely on signals from the Global Positioning Service (GPS), and field experiments could demonstrate that information from such systems can measure sea level with an accuracy of a few centimeter. However, the usage of the Russian GLONASS system has the potential to simplify the processing scheme and to allow handling of direct and reflected signals like a bistatic radar. Thus, such a system has been developed and deployed for test purposes at the Onsala Space Observatory, Sweden, that has an operational GPS-based GNSS-R system. Over a period of two weeks in October 2013, GPS-based GNSS-R sea-level monitoring and measurements with the newly developed GLONASS-R system were carried out in parallel. In addition, data from co-located tide gauge measurements were available for comparison. It can be shown that precision and accuracy of the GLONASS-based GNSS-R system is comparable to, or even better than, conventional GPS-based GNSS-R solutions. Moreover, the simplicity of the newly developed GLONASS-R system allows to make it a cheap and valuable tool for various remote sensing applications.

1. Introduction

Global Navigation Satellite Systems (GNSS) have not only revolutionized positioning, navigation and timing but also lead to the development of many other applications which were not anticipated when those satellite systems were designed decades ago. The most prominent example for a novel application from recent years is the usage of reflected GNSS signals as a new tool for remote sensing. This method, called GNSS-Reflectometry (GNSS-R), operates like a bi-static radar [*Willis*, 2007] and allows to derive geometric and physical properties of the reflecting surface. GNSS-R observations can be either performed with a single antenna, or with two antennas, one up- and one down-looking, which are receiving direct and reflected signal separately. Single antenna configurations are usually selected when existing geodetic GNSS infrastructure is utilized, and no dedicated GNSS-R system is deployed in the field. In doing so, such systems can provide sea-level height (e.g. *Larson et al.* [2013] or *Löfgren et al.* [2013a]), snow depth (e.g. *Larson and Nievinski* [2013]) or soil moisture information (e.g. *Larson et al.* [2008]) by analyzing certain multi-path characteristics of the received signals. Dedicated GNSS-R systems which operate with two antennas have the advantage of receiving signals separately and thus allow for a more sophisticated signal processing. However, such systems are not built with off-the-shelf components but are usually dedicated hard- and software solutions which handle all necessary processing steps. In particular, standard off-the-shelf GNSS antennas are sold only with a high sensitivity for right-hand circular polarized (RHCP) radio frequency (RF) signals and a significant attenuation for left-hand circular po-

larized (LHCP) signals. However, direct GNSS signals are received in RHCP, but reflected signals change their polarization and reach the antenna in LHCP. Thus, one needs to make sure that the second antenna, which is dedicated to the reception of reflected signals, has a high sensitivity for LHCP and a strong attenuation for RHCP signals. Most of the dual antenna GNSS-R systems are deployed so that the RHCP antenna points towards the sky and the LHCP is oriented downwards or at least being tilted towards the horizon in order to receive the reflected signals within the main lobe of the antenna beam. Depending on the application and the area of interest, such systems are mounted close to the ground (e.g., *Löfgren et al.* [2011]), flown on an airplane (e.g., *Garrison et al.* [1997]) or even installed on board of a satellite (e.g., *Gleason et al.* [2005]). However, all these applications have in common that the received GNSS signals, both the direct and reflected one, need to be correlated against the replica of the transmitted signal. This restriction applies to most GNSS as they transmit their signals via a Code Division Multiple Access (CDMA) scheme. CDMA allows to transmit several specially designed Pseudo Random Noise (PRN) codes on the same carrier frequency, without interfering with each other. Thus, correlation of direct and reflected signals, which is required for a bi-static radar application, is not directly realizable with a CDMA based receiver. As discussed in *Rius et al.* [2012] there are three ways to overcome this limitation. One could use Doppler shifts to distinguish between the satellites or add a time gating function that selects data only within a time window of the expected delay. However, both methods only work if either the Doppler shift or the time delay of the reflected signal w.r.t. the direct one

are significant, which is only feasible if such an interferometric GNSS-R system is put on a satellite. The third method demonstrated in *Rius et al.* [2012], uses antenna directivity, which selects a signal from a single satellite and assigns it to a correlation channel. Although the results from this approach seem to be very promising for sea level monitoring, the problem remains that such a system requires dedicated hardware and strongly depends on the beam steering capabilities of the receiving antennas.

2. The GLONASS-R concept and its realization

The Russian GLONASS system does not rely on the CDMA scheme for distinguishing between satellite transmitters, unlike the U.S. Global Positioning (GPS), the European Galileo system or the Chinese BeiDou Navigation Satellite System. In general, each GLONASS satellite transmits on a different frequency, using a 15-channel Frequency Division Multiple Access (FDMA) technique spanning both sides from the GLONASS L1 center frequency. Thus, using only a single PRN code, satellites can be only distinguished by their allotted frequency. If $(n = -7, -6, \ldots, 5, 6)$ is the satellite's frequency channel number the corresponding transmission center frequency f_n for each satellite can be calculated by

$$f_n = 1602 \, \text{MHz} + n \cdot 0.5625 \text{MHz}. \tag{1}$$

As there are only 15 unique channels, identical channels are assigned in a way that antipodal satellite pairs share the same n. In doing so, satellites transmitting at the same frequency channel will never be in view of an earth-based user at the same time.

The civil and military navigation signals transmitted on L1 are bipolar phase-shift key (BPSK) waveforms with clock rates of 0.511 MHz and 5.11 MHz, respectively. Although the bandwidth of the military codes is much wider than the 562.5 kHz spacing of each channel, it is known that the signal contribution of a single transmitter n is dominating inside the frequency range $[f_n - 281.25\,\text{kHz}, f_n + 281.25\,\text{kHz}]$. GLONASS signals have been used for GNSS-R purpose before as discussed in *Löfgren et al.* [2013b]. But signal processing has been performed like for GPS, i.e. with standard geodetic GNSS receivers where RHCP and LHCP signals are correlated separately against the replica codes after band-pass filtering the corresponding frequency channels.

Since the GLONASS satellites are distinguishable in the frequency domain the idea of realizing a GLONASS based interferometric GNSS-R system, hereafter named "GLONASS-R", has been pursued. Figure 1 depicts how such a system can be realized. Direct (RHCP) and reflected (LHCP) signals are down-converted, analog-to-digital (A/D) converted, and then transformed into the frequency domain. As signals from different satellites are located at different frequencies, one can easily select a satellite by applying a filter with a pass-band that corresponds to the frequency range of the GLONASS channel. Instead of filtering the two signals separately, one can make use of the Fourier representation and compute the cross-spectrum of both signals first and then apply the band-pass filter. In doing so, a simple inverse Fourier transformation after the filtering provides the cross-correlation function, i.e. the time delay between the direct and reflected signal. However, it has to be taken into ac-

count that the application of such a narrow band-pass filter leads to a broadening of the cross-correlation function around its peak. As the delay precision is inversely proportional to the bandwidth it is obvious that such an observable cannot provide sub-meter accuracy. On the other side, it is possible to use the phase, derived from the cross-spectrum, in order to measure the delay of the reflected signal with respect to the direct one. The precision of such an interferometric phase observable is about 100 times better than the delay obtained from the cross-correlation function. The two remaining problems are the phase unwrapping and the determination of an ambiguity for each satellite pass (see Sect. 2.3). In addition, also the correlation amplitude can be derived, which can be used as another observable or used for data-weighting in the data analysis.

2.1. RF front-end and A/D converter

For a GNSS-R system operating with two different antennas, it is crucial that signal conversion or processing is done coherently throughout the whole system. This aspect and the requirement that the whole GLONASS L1 band in the radio frequency (RF) has to be down-converted to a base-band frequency range for the A/D conversion, need to be considered for designing the front-end for the GLONASS-R system. Considering these prerequisites, a dedicated hardware front-end for the proposed GLONASS-R system has been designed and assembled (cf. Fig. 2). The RHCP and LHCP RF signals are band-pass filtered and coherently mixed-down to base-band. In order to make sure that this coherency is preserved throughout the analog signal chain, the same 10 MHz signal which is used for the down-conversion,

i.e. the phase-locked oscillators (PLO), is also driving the analog to digital converter, which samples both signals with a frequency of 64 MHz in one-bit representation. The PLOs are selected in a way to make sure that the nominal GLONASS L1 RF is down-converted to the center of the 32 MHz wide spectrum (i.e. at 16 Mhz) covered by the A/D sampler. The latter had been designed originally for Very Long Baseline Interferometry (VLBI) [*Kondo et al.*, 2006]. The one-bit resolution ensures that RHCP and LHCP signals can be transmitted in real-time via the Universal Serial Bus (USB) 2.0 protocol to a standard off-the-shelf PC for further processing.

2.2. Graphic Processing Unit (GPU) based software radio

Since the GLONASS-R concept can neither be realized by commercial GNSS receivers nor by other existing hardware, a cheap, flexible and easy to implement solution had to be found. Other than hardware solutions or Field Programmable Gate Arrays (FPGAs), a software defined radio fulfills all these requirements, given that the incoming digital data-stream can be handled in real-time. Thus, an important consideration is that signal processing should be performed while data is streamed from the sampler to the PC, keeping at least one CPU core busy with this data handling process. Based on the experience from prior studies [*Hobiger et al.*, 2010, 2012] with graphic processing units (GPU), the GLONASS-R signal processing chain has been implemented on a GPU. This allows not only to relieve the CPU from the resource demanding signal processing operations, but also benefits from the massive parallel processing power of a GPU. Based on the Compute Unified Device Architecture (CUDA, *Sanders and Kandrot* [2010]) and highly optimized Fast Fourier Transfor-

mations (FFTs) from *NVIDIA* [2013] a straightforward and flexible implementation of the GLONASS-R concept becomes feasible.

Figure 3 depicts the GLONASS-R signal processing which can be implemented on a standard off-the-shelf PC. A CPU thread listens to the USB port which connects to the sampler, splits the incoming packages into RHCP and LHCP signals and puts the data stream in two separate circular buffers in CPU memory. The size of these buffers is selected so that at least 30 seconds of continuous sampling are stored at any time. The rest of the processing is done on the GPU and can be summarized as follows. If the GPU is idle, it copies one second of RHCP and LHCP data to the GPU memory and performs parallel streamed FFTs on RHCP and LHCP signals, where each FFT batch equals to a length of one millisecond. Thereafter, the cross-spectrum is computed and coherently integrated. In addition, amplitudes of the cross-spectrum are summed up and integrated in order to normalize the cross-spectrum at a later stage. After one second of data has been processed, the integrated spectrum remains in GPU memory and another one-second batch of data is copied to the GPU memory, processed in the same way and added to the cross-spectrum, and so on. After coherent integration over a user-defined interval of T seconds, a band-pass with a width of $\Delta f = 526.5\,\mathrm{kHz}$ is applied for each GLONASS satellite i and the cross-correlation function is obtained by an inverse Fourier transformation. The location of the peak defines the time-delay τ_i of the reflected signal w.r.t. the direct signal. Using this information, the phase slope $\tau_i = \partial\phi_i/\partial f_i$ in the cross-spectra can be compensated, before computing the sum of real $S_{Re,i}$ and imaginary components $S_{Im,i}$ of the nor-

malized cross-spectrum. Since only FFT points inside the band-pass are considered, this operation can provide the necessary information for each GLONASS channel. In doing so, the relative phase ϕ_i and the cross-correlation amplitude ρ_i can be extracted by

$$\phi_i = \arg\left(\frac{S_{Im,i}}{S_{Re,i}}\right) \tag{2}$$

and

$$\rho_i = \sqrt{(S_{Re,i})^2 + (S_{Im,i})^2}. \tag{3}$$

Once delays, phases and amplitudes are obtained for all GLONASS channels, these results are copied back to the CPU where they are time tagged and stored in ASCII files. After this, the coherent integration buffer of the cross-spectrum is reset and the GPU thread processes the next one second batch of data. Since the GPU thread easily catches up with a data rate of 64 mega-samples per second (Msps), all channels, irrespective of the satellite visibility, would be processed in real-time. If the location of the GLONASS-R system is known, one can reduce the computational burden and select only those frequency channels which correspond to satellites that are visible at this site. In order to support this feature, geocentric antenna coordinates as well as satellite orbits, in the form of two-line element (TLE) parameters [*CelesTrak*, 2013], can be input to the software receiver, which then only processes those satellites which are above the local horizon, or within a user-defined azimuth/elevation mask.

2.3. Post-processing

Given that the GLONASS-R system is not mounted on a moving platform and the height above the reflecting surface is small enough so that relative Doppler shifts

can be neglected post-processing and interpretation of the observations can be done straightforward. In case the platform is moving, a more complex processing scheme would be required as discussed in Sec. 5.

Code phase, i.e. group delay, measurements of a standard GNSS receiver, which correlates the incoming signal against a noise-free replica signal, are known to have a precision of several meters. Thus, one can expect that for the GLONASS-R system which correlates directly two noisy and narrow-band GNSS signals, one of them being even weaker after the reflection, the precision of delay measurements τ_i is not sufficient for a meaningful determination of geometric properties of the reflecting surface. Therefore, carrier phase measurements remain as the only meaningful observable for such GNSS-R applications, given that the reflecting surface is smooth enough to preserve phase coherence. However, the usage of carrier phase measurements raises the complexity of post-processing because the raw phases measurements $\phi_i \in [-\pi, \pi]$ need to be unwrapped before they can be used. As long as the signal-to-noise ratio is high enough, this can be easily achieved by detecting jumps larger than a certain threshold and then connecting the consecutive phases by adding $\pm 2\pi$. Unwrapped phases are denoted by ϕ_i^* hereafter. The second complication that arises with using phase observations is caused by the fact that although phases can be connected consecutively throughout one satellite passage, an unknown offset remains in each of these arcs. This bias needs to be estimated together with the altimetry information, i.e. the height above the reflector.

If a plane and horizontal reflecting surface is assumed, one can relate the interfer-

ometric delay Δd, expressed as a distance, directly to the bi-static radar geometry as depicted in Fig. 4. Considering that the elevation angle ε can be computed from station position and orbit information, this relation is

$$\underbrace{\Delta d_1 + \Delta d_2}_{\Delta d} = (2h + \delta) \cdot \sin \varepsilon, \tag{4}$$

where δ is the vertical distance of the two antenna phase centers and h is the height of the downward looking antenna above the reflecting surface. Absolute phase center models for GLONASS capable antennas are available with mm-accuracy [*Dach et al.*, 2011] and the spacing of the two antennas can be measured directly. Rewriting Equation 4 for satellite i, introducing a time-dependency t and recalling that the unwrapped phase measurements $\phi_i^*(t)$ (expressed in units of length) contain an unknown, but constant bias $\Delta\phi_i$, the observation equation becomes

$$\phi_i^*(t) = 2h'(t) \cdot \sin \varepsilon_i(t) + \Delta\phi_i, \tag{5}$$

where $h' = h + \frac{\delta}{2}$ is the virtual height above the reflector. The estimation of the unknowns, i.e. $h'(t)$ and a constant bias for each satellite passage, is possible if observations at different elevation angles from several satellites are used together. If data are analyzed in real-time, a Kalman filter approach [*Kalman*, 1960] can be used for estimating the height above the reflecting surface together with the arc biases $\Delta\phi_i$. For off-line post-processing, as discussed in the next sections, a least-squares adjustment based on a Gauss-Markov model [*Koch*, 1997] can provide these estimates, given that $h'(t)$ is parameterized by a suitable representation which allows to model temporal changes of the reflecting surface.

2.3.1. Parameterization of reflector height variations

Changes of the reflector height, in particular the ocean surface which was observed in the field experiment described in Section 3, are expected not to happen suddenly nor to contain any discontinuities. Instead one can assume that the probed surface varies continuously or shows a periodic behavior. Therefore, a simple functional model is required, that relies only on a few parameters, but resolves temporal changes at a user-defined resolution. In this work, the quadratic B-spline function is used, and its scaling coefficients are determined by an adjustment process. Given positive integers d and k, with $k \geq d$, and a collection of non-decreasing values $t_0, t_1, \ldots, t_{k+d+1}$ called knots, the non-uniform B-spline basis functions of degree d are defined recursively [*Stollnitz et al.*, 1995]. For $j = 0, 1, \ldots, k$, and for $r = 1, \ldots, k$, let

$$N_j^0(t) = \begin{cases} 1 & \text{if } t_j \leq t < t_{j+1} \\ 0 & \text{otherwise} \end{cases} \tag{6}$$

$$N_j^r(t) = \frac{t - t_j}{t_{j+r} - t_j} N_j^{r-1}(t) + \frac{t_{j+r+1} - t}{t_{j+r+1} - t_{j+1}} N_{j+1}^{r-1}(t) \tag{7}$$

(Note: The fractions in Equation 7 are set to zero when their denominators are zero). So-called endpoint-interpolating B-splines of degree d on the interval $[t_A, t_B]$ can be obtained when the first and last $d+1$ knots are set to t_A and t_B, respectively. In the following, quadratic B-splines $N_j^2(t)$ in the interval $t \in [t_{start}, t_{end}]$ are used, where t_{start} and t_{end} denote the start and end time of a GLONASS-R field experiment. In addition, equally spaced knots with a temporal resolution of three hours are chosen, covering the main sub-daily ocean and atmosphere tidal modes.

2.3.2. Parameter estimation and data-weighting

The weighting of each data-point is important since the precision of phase measurements can change rapidly, depending on the physical properties of the reflecting surface. In most cases an elevation dependency can be observed, which is caused by the antenna beam pattern and the bi-static radar geometry. However, other factors, e.g. sea surface roughness, can decrease phase precision when coherent integration is performed over an interval during which the interferometric phase is changing by more than a few degrees. Thus, instead of using an empirical model, e.g. elevation dependency, for data weighting, it is better to rely on the formal errors, which can be assigned to each phase measurement. As described by *Takahashi et al.* [2000], the standard deviation of angular phase measurements is inversely proportional to their signal-to-noise ratio (SNR), i.e.

$$\sigma_{\phi_i} = \frac{1}{\mathrm{SNR}_i}. \tag{8}$$

Knowing that the SNR can be computed from the correlation amplitude ρ_i, the bandwidth B and the integration length T as follows

$$\mathrm{SNR}_i = \rho_i \sqrt{2BT}, \tag{9}$$

the stochastic model for the parameter adjustment can be set-up straightforward. Considering that only relative weights are needed, the factor $\sqrt{2BT}$ can be omitted because all GLONASS channels were processed with the same band-pass filter and the integration was performed over the same period of time. Since weights are inversely proportional to the variance, i.e. $1/\sigma_{\phi_i}^2$ and observations are assumed to be

uncorrelated, the weight matrix can be expressed by

$$W_{nm} = \begin{cases} \rho_i^2 & (n, m = i) \\ 0 & (n \neq n) \end{cases} \tag{10}$$

If $h'(t)$ is approximated by quadratic B-splines $N_j^2(t)$, Equation 5 becomes

$$\phi_i^*(t) = 2 \sin \varepsilon_i(t) \cdot \sum_{j=0}^{M} \alpha_j N_j^2(t) + \Delta\phi_i, \tag{11}$$

where α_j are the scaling coefficients for the corresponding B-spline functions with M nodes. Since the model is linear in all its unknowns, a weighted least-squares estimation can provide both the unknown phase offsets $\Delta\phi_i$ and the functional approximation of temporal reflector height variations.

2.3.3. Back-substitution of estimated phase offsets for higher temporal resolution

As discussed in the previous section, the temporal resolution of the B-spline approximation of $h'(t)$ is limited by the number of nodes and their temporal separation. A denser node spacing could better model short-term variations, but leads to a larger number of unknowns and makes it more difficult to de-correlate the B-spline coefficients α_j from the phase offsets $\Delta\phi_i$. The latter may cause wrong height estimates, especially when arcs of continuous phase tracking are short and observations are less precise. A possible solution for a better temporal resolution, down to the original coherent integration length, can be achieved by a two-step approach. First, the estimation process as suggested in Sec. 2.3.1 is carried out, estimating B-spline coefficients and phase offsets. In the second step, the phase offsets determined in the

first step are used to solve for $h'(t)$ directly, i.e. rearranging Eq. 5 to

$$h'(t) = \frac{\phi_i^*(t) - \Delta\phi_i}{2\sin\varepsilon_i(t)}. \tag{12}$$

Although Eq. 12 can be used to obtain $h'(t)$ for every satellite passage separately, it is better to compute a weighted mean over all satellites which were tracked at the same epoch, i.e.

$$h'(t) = \frac{\displaystyle\sum_{t=t_i} \rho_i^2 \frac{\phi_i^*(t) - \Delta\phi_i}{2\sin\varepsilon_i(t)}}{\displaystyle\sum_{t=t_i} \rho_i^2}, \tag{13}$$

where amplitudes ρ_i are used as realistic weights for the combination of the different observations.

3. Field tests at the Onsala Space Observatory

In order to validate the GLONASS-R concept, a field test of a prototype system at a coastal site was planned. Operating the GLONASS-R system as an altimeter does not only allow assessing the precision of the instrument, but also makes it possible to evaluate its accuracy by comparing with external measurements, e.g. from a tide gauge. A potential site for the deployment of the prototype system should be easily accessible and has to provide the necessary infrastructure, like power, Internet access and stable 10 MHz reference and one-pulse-per-second (1 PPS) signals. In addition to these requirements, the range of potential test sites was limited to only those locations where a conventional GNSS-R system is operational and such data can be used to judge the quality of the GLONASS-R concept.

3.1. Site description

The Onsala Space Observatory (OSO), located on the Swedish west coast, about 40 km south of Gothenburg, operates a GNSS-R system since several years [*Löfgren et al.*, 2011]. Regularly the local sea-level at the site is monitored and experiments are conducted that aim to improve the accuracy and precision of GNSS-R. Figure 5 shows a picture of the GNSS-R installation at Onsala, where a beam holding RHCP and LHCP antennas above the sea is mounted on solid bedrock. Additionally, a pneumatic tide gauge [*Pugh*, 1972] is installed close to the GNSS-R antennas, which allows comparison and validation of sea level results. Therefore, this site was selected for testing and validation of the GLONASS-R concept. The necessary components (PC, RF front-end and A/D converter) were shipped from Japan to Onsala and deployed at the site in the beginning of October, 2013. Active splitters were inserted in the RF signal path in order to be able to use the RF signals in parallel for the receivers of the OSO GNSS-R installation and the GLONASS-R system. Moreover, a 10 MHz and a 1 PPS signal were provided, so that down-conversion and sampling could be done coherently.

As shown on the aerial image in Fig. 6, reflections from the azimuth range between 90° and 280° can be received at any elevation angle. As the beam that holds the GNSS antennas extends out from the shoreline over the open sea by about 2 meters, even reflections from the northern sky can be processed if an elevation cut-off angle of 55° is applied to that sector.

3.2. Results and comparison

The length for coherent integration (cf. Sec. 2.2) was set to $T = 5$ s, which provides enough SNR for obtaining meaningful phase observations and allows to access even very short temporal variations of the sea surface. The GLONASS-R system was set-up to track all satellites down to an elevation angle of 5°. Although observations at lower elevation angles provide low SNR and thus are treated with less weight in the adjustment process (cf. Eq. 10), the phase information from those elevations accounts for a large portion of the total amount of data. To prevent that these less precise observations influence the quality of the altimetry solution, an empirically determined cut-off angle of 35° was applied in the post-processing. Based on these settings, the GLONASS-R prototype system was started on Oct. 10th, 2013, for a continuous 11-day measurement campaign. The first five days of continuous operation of the GLONASS-R system went without any problems, before a failure of the sampler software, which was detected with some delay, lead to a one day long data gap. As a similar failure happened again after restart and a few hours of continuous operations, the system was shut down on Oct. 16th and the code of the sampler module was changed in order to avoid that missing A/D samples lead to a memory leak of the software receiver. After this bug-fix the system ran smoothly until the end of the field campaign, i.e. Oct. 21st, 2013. However, in order to test the impact of different values of the coherent integration lengths T (cf. Sec. 3.2.3), the software radio was operated during of a few hours with different settings for T, which led to a third gap in the time series of results obtained with 5 second integration

time. Data from the pneumatic tide gauge were available throughout the 11 days long campaign with a sampling rate of 60 seconds. The conventional GNSS-R system at OSO was unfortunately by mistake not in operation during the first days of the campaign, and thus results from this system could only be used as an additional source for validation for the time after Oct. 16, 2013.

3.2.1. GLONASS-R results

After unwrapping GNSS-R raw phase observations and removing data below the elevation cut-off mask, the height of the LHCP antenna above the sea surface was estimated with the methods described in Sec. 2.3. First a smoothed solution, hereafter called GLONASS-R (BSP), was calculated, based on the three-hourly B-spline approach (see Sec. 2.3.1) . Then the estimated phase offsets of the first solution were re-used (cf. Sec. 2.3.3) in order to obtain a time series of GLONASS-R altimetry measurements with a temporal resolution that is equal to the coherent integration length, i.e. 5 seconds, respectively 0.2 Hz. Both solutions are plotted in Figure 7 together with other measurement data, which are described in the next sections. Beside the data-gaps, which were explained in the previous section, larger scatter is detected for data collected on Oct. 19th, 2013. Although the B-spline solution appears to be reasonable around this period at first glance, it can be seen that this approach smoothes the high-rate results, but does not reveal any smaller physical signal caused by a change of sea surface height. A comparison with wind-speed measurements (see lower plot in Fig. 7) reveals that the period of large scatter coincides with high wind velocities observed at OSO. As wind-speed strongly correlates with sea surface

roughness, the latter can explain why the performance of the GLONASS-R system degrades during that period.

3.2.2. Comparison against tide gauge data and performance of a GPS based GNSS-R system

For the validation of the back-substituted GLONASS-R time-series, observations from the pneumatic tide gauge were available throughout the whole duration of the field campaign. Additionally, two GPS-based GNSS-R time-series were available, derived from the standard OSO GNSS-R installation, but only for the second half of the campaign. The first one was obtained from analyzing the direct and reflected GPS L1 phase measurements [*Löfgren et al.*, 2011] received with the up- and downward antenna, respectively, while the second one was obtained with the SNR method [*Larson et al.*, 2013], using only data from the up-ward looking antenna. Outliers of the GPS L1 phase solution were removed by two criteria. First, all data-points which had a formal error larger than 4 cm, were rejected. Second, a running mean filter with a window size of 3.5 hours was applied in order to generate a smoothed time-series which was then used as reference to detect further outliers by applying a 3-sigma criteria around that filtered series. As no formal errors are available for SNR based sea level height measurements, the outliers from this time series were only removed by a 3-sigma criteria. Again, a filtered series with a window length between 2.5 and 4 hours, depending on the temporal resolution of the SNR solution, was taken as reference for such an outlier rejection. Both GPS-based time-series are presented together with the GLONASS-R results and the tide gauge measurements

in Figure 7. Individual mean values have been subtracted from each time series, and to improve the readability of the figure the time series are presented with offsets of 20 cm.

During the period with strong wind (Oct. 19), the GPS phase solution has a data gap. Either loss-of-lock occurred for the commercial geodetic receiver that was connected to the LHCP antenna, or the solutions during that period were rejected by the post-processing outlier criteria. Similarly, for the GLONASS-R system, a rougher sea surface and thus a worse phase coherence is suspected to be the reason for the performance degradation during that period. In order to elaborate more on this issue, epochs with certain wind speed ranges were defined and then the root-mean-square errors (RMSE) w.r.t. the pneumatic tide gauge measurements were computed for the two GPS solutions and for the GLONASS-R measurements. The histogram depicted in Figure 8 summarizes these results, showing a clear wind speed dependence of both GLONASS-R and the GPS L1 phase based reflectometry systems. On the contrary, the SNR based GNSS-R sea level height measurements seem to be less affected by wind speed and the corresponding change of sea surface roughness. However, at much higher wind speeds the spatial coherence will deteriorate to such extent that the GPS SNR approach would not work either. Thus, sea surface roughness sets an implicit limit for any system used at the OSO test site. Among the systems used in this study, the GLONASS-R system performs slightly better than the GPS L1 phase observations, which can be explained by the fact that GLONASS-R software radio does neither rely on a delay-locked loop (DLL) nor on a phase-locked loop (PLL) and

thus is less affected by improper tracking of observations with low SNR.

For a calm sea surface, i.e. wind speeds less than 2 m/s, the GLONASS-R system appears to be capable to reach an accuracy of about $1-2$ cm which is about $30-50$ % better than the performance obtained by a GPS based GNSS-R system as reported by *Löfgren et al.* [2011]. Given that outliers in the back-substituted GLONASS-R time-series are not eliminated and no averaging process has been applied, sea-level height observations with an RMS accuracy of one centimeter seem to be feasible. However, for better evaluation of the instrument's precision and accuracy and a more conclusive comparison among the different systems a longer time-span, providing more data-points to each wind speed category, would be needed.

3.2.3. Choice of the integration length

As implicitly expressed in Eq. 8 and Eq. 9, the phase measurement precision can only be improved by two means, either by extending the integration length T or by broadening the used bandwidth B. As the latter is impossible due to the limited channel-width of a single GLONASS transmitter of 562.5 kHz, only the integration time can be modified in order to obtain less noisy phase observables. Given that precision follows $\sim 1/\sqrt{T}$ it is clear that doubling the integration length only gains a 30 percent improvement in measurement precision. Moreover, it has to be considered that during integration it is required that the phase does not change by more than a few degrees, otherwise coherence losses will start to degrade the precision of the observable. In order to evaluate the impact of the integration length on the performance of the GLONASS-R system, tests with integration lengths of 1, 3, 5 and 10

seconds were performed on Oct. 18th, 2013, at the OSO GNSS-R site. Each test was carried out over a period of one hour and only observations with an elevation angle larger than $55°$ were used. The latter restriction allows us to compare the test runs, which have a different satellite geometry, without biasing the conclusions by an elevation dependent system performance. In post-processing the obtained phase observations were unwrapped and used to estimate the height of the LHCP antenna above the sea surface with the B-spline method (cf. Sec. 2.3.1), where only two nodes, i.e. at the beginning and the end of each hourly data set, were parameterized. This means that implicitly a single quadratic polynomial was used to model $h'(t)$ for each data set. In order to evaluate the impact of the integration length, the RMSE of the residuals w.r.t. the estimated model was computed. Figure 9 depicts these values together with the model

$$\sigma = \frac{A}{\sqrt{T}}, \tag{14}$$

where the coefficient A was determined by a fit to 0.02 meter. It can be seen that the observed measurement precision follows closely $\sim 1/\sqrt{T}$, as predicted by Eq. 8 and Eq. 9. However, this law might be violated for longer periods, especially when the phases change rapidly within the coherent integration time. On the other hand, shorter integration times than one second will not follow the $\sim 1/\sqrt{T}$ rule either, since noisier phase measurements will prevent a successful unwrapping of all phase observations belonging to one satellite pass. Given the results depicted in Fig. 9, a 5 second integration time for the initial field tests described in the prior sections, seemed to be a good trade-off between temporal resolution and obtained measurement precision.

Moreover, it has to be considered that the estimation of B-spline coefficients, or the use of any other approximating function, implicitly averages measurements over a certain interval of time and thus also influences the precision and consequently the formal error of the model representation for $h'(t)$, according to $\sim 1/\sqrt{T}$.

4. Conclusions

The feasibility of the GLONASS-R concept was proven in a field experiment at the OSO, Sweden, and it could be demonstrated that such an interferometric system can provide sea surface height measurements with an accuracy that is comparable or even better than conventional GNSS-R systems. Although the GLONASS-R approach requires a special signal processing chain, its simplicity allows to realize such a system by means of software defined radio. Thus, based on standard off-the-shelf components and exploiting the parallel processing power of a GPU, such a system can be operated in real-time. For calm sea surface conditions, the GLONASS-R prototype reached an accuracy of about $1 - 2$ cm, outperforming other GNSS-R systems at that site. In case of rough swell, GLONASS-R still performs better than the GPS L1 phase based system, but is not as accurate as sea surface heights derived from SNR measurements. This drawback might be overcome in future experiments, as described in the next section.

5. Outlook

In order to avoid degraded performance when the sea surface gets rough, a dynamic control of coherent integration length is proposed. In case of rough swell, longer

integration periods could be selected, leading to a coarser temporal resolution, but significantly improving the accuracy of the system during such periods. This can be implemented straightforward by controlling the integration time in accordance with external measurements, e.g. data from wind speed sensors. As the cross-spectrum is integrated continuously, only the integration period has to be modified after which the spectrum is used to determine delays, phases and amplitudes of all GLONASS channels (cf. Sec. 2.2). The flexibility of a software defined radio allows to adopt the signal processing chain to this new scheme very easily.

Even further modifications of the coherent integration length can be implemented. Satellites at high elevation angles are usually received with higher SNR as the antenna antenna beam pattern supports such observations better than at low elevation. This leads to the idea of dynamically adopting the integration period individually for each satellite. Satellites at lower elevations can have longer integration times in order to compensate for lower signal strength at those elevation ranges. This dynamic control can be implemented again with only minor changes in the software-defined signal processing chain, and is anticipated to be tested in one of the next field campaigns. Given its simplicity, the GLONASS-R concept might also be of use for air- or space-borne interferometric GNSS-R instruments [*Cardellach et al.*, 2013]. For such applications it would be necessary that the Doppler shift and spread of the reflected signal are handled properly and aircraft altitude is tracked and compensated with sufficient accuracy. This would then allow a straightforward determination of so-called delay-Doppler maps [*Rodriguez-Alvarez et al.*, 2013], which can be used for a variety of

geophysical applications.

However, all possible advantages have to be seen under the long term plan of the Russian Aerospace Defense Forces which operates the GLONASS system. As the system modernization plan [*Revnivykh*, 2012] foresees the transmission of navigation signals via the CDMA technique, it is not clear if and how this would impact the realization of the GLONASS-R concept.

References

Cardellach, E.,A. Rius, M. Martín-Neira, F. Fabra, O. Nogués-Correig, S. Ribó, J. Kainulainen, A. Camps, and S. D'Addio (2013), Consolidating the Precision of Interferometric GNSS-R Ocean Altimetry using Airborne Experimental Data, *IEEE Transactions on Geoscience and Remote Sensing*, *in print*, doi: 10.1109/TGRS.2013.2286257.

CelesTrak (2013), NORAD Two-Line Element Sets, *http://www.celestrak.com/*.

Dach, R., R. Schmid, M. Schmitz, D. Thaller, S. Schaer, S. Lutz, P. Steigenberger, G. Wübbena, and G. Beutler (2011), Improved antenna phase center models for GLONASS, *GPS Solutions*, *15*(1), 49–65, doi:10.1007/s10291-010-0169-5.

Garrison, J.L. and S.J. Katzberg (1997), Detection of ocean reflected GPS signals: theory and experiment, *Proceedings of the IEEE Southeastern '97: Engineering the New Century[C], Blacksburg, Virginia*, 290–294, doi: 10.1109/SECON.1997.598694.

Gleason, S., S. Hoodgart, Y. Sun, C. Gommenginger, S. Mackin, M. Adjrad, and M. Unwin (2005), Detection and processing of bistatically reflected GPS signals from low Earth orbit for the purpose of ocean remote sensing, *IEEE Trans. Geosci. Remote Sens.*, *43*(6), 1229–1241, doi:10.1109/TGRS.2005.845643.

Hobiger, T., T. Gotoh, J. Amagai, Y. Koyama, and T. Kondo (2010), A GPU based real-time GPS software receiver, *GPS Solutions*, *14*(2),207–216. doi: 10.1007/s10291-009-0135-2.

Hobiger, T., J. Amagai, M. Aida, and H. Narita (2012), A real-time GNSS-R system based on software-defined radio and graphics processing units, *Advances in Space Research*, *49*(7), 1180–1190, doi:10.1016/j.asr.2012.01.009.

Kalman, R. E. (1960), A New Approach to Linear Filtering and Prediction Problems,, *Transactions of the ASME–Journal of Basic Engineering*, *82*(D), 35–45.

Koch, K.R. (1997), *Parameter Estimation and Hypothesis Testing in Linear Models*, Springer, Berlin.

Kondo, T., Y. Koyama, H. Takeuchi, and M. Kimura (2006), Development of a New VLBI Sampler Unit (K5/VSSP32) Equipped with a USB 2.0 Interface, *International VLBI Service for Geodesy and Astrometry 2006 General Meeting Proceedings, edited by Dirk Behrend and Karen Baver*, NASA/CP-2006-214140, 195–199.

Larson, K. M., E. E. Small, E. Gutmann, A. Bilich, J. Braun, and V. Zavorotny (2008), Use of GPS receivers as a soil moisture network for water cycle studies, *Geophys. Res. Lett.*, *35*, L24405, doi:10.1029/2008GL036013.

Larson, K. M., J. Löfgren, and R. Haas (2013a), Coastal Sea Level Measurements Using A Single Geodetic GPS Receiver, *Adv. Space Res.*, *51*(8), 1301–1310, doi: 10.1016/j.asr.2012.04.017.

Larson, K. M. and F. G. Nievinski (2013b), GPS Snow Sensing: Results from the EarthScope Plate Boundary Observatory, *GPS Solutions*, *17*(1), 41–52, doi: 10.1007/s10291-012-0259-7.

Löfgren, J. S., R. Haas, H. G. Scherneck, and M. S. Bos (2011), Three months of local sea level derived from reflected GNSS signals, *Radio Science*, *46*(6), doi: 10.1029/2011RS004693.

NVIDIA (2013), The CUFFT library user guide, *http://docs.nvidia.com/cuda/cufft/*.

Pugh, D. T. (1972), The physics of pneumatic tide gauges, *International Hydrographic Review*, *49*(2), 71–97.

Revnivykh, S. (2012), GLONASS: Status and Modernization, International GNSS Committee IGC-7 Beijing, 4-9 November, *http://www.unoosa.org/pdf/icg/2012/icg-7/3-1.pdf*.

Rius, A. , O. Nogues-Correig, S. Ribo, E. Cardellach, S. Oliveras, E. Valencia, H. Park, J. Tarongi, A. Camps, H. Marel, R. Bree, B. Altena, and M.=Martin-Neira (2012), Altimetry with GNSS-R interferometry: first proof of concept experiment, *GPS Solutions*, *16*(2), 231–241, doi:10.1007/s10291-011-0225-9.

Rodriguez-Alvarez, N., D. M. Akos, V.U. Zavorotny, J.A. Smith, A. Camps, and C.W. Fairall (2013), Airborne GNSS-R Wind Retrievals Using DelayDoppler Maps, Geoscience and Remote Sensing, *IEEE Transactions on Geoscience and Remote Sensing*, *51*(1), 626–641, doi:10.1109/TGRS.2012.2196437

Sanders, J., and E. Kandrot (2011), *CUDA by Example - An Introduction to General-Purpose GPU Programming*, Addison Wesley.

Stollnitz, E. J., T.D. DeRose, D.H. Salesin (1995), Wavelets for computer graphics: A primer, part 2, *IEEE Computer Graphics and Applications*, *15*(4), 75–85, doi: 10.1109/38.391497.

Takahashi, F., T. Kondo, Y. Takahashi, and Y. Koyama (2000), *Very Long Baseline Interferometer*, Ohmsha, Ltd., Japan.

Willis, N. (2007), *Bistatic Radar*, SciTech Publishing. 2nd ed, ISBN 1-891121-45-6.
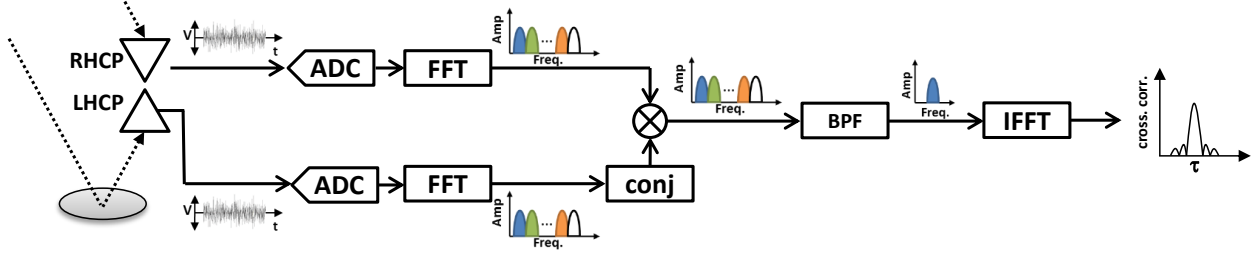
Figure 1. Illustration of the GLONASS-R concept. After reception by RHCP and LHCP antennas and an analog-to-digital (A/D) conversion, Fourier representation of each signal can be obtained. A GLONASS satellite can be selected by applying a band-pass filter (BPF) that covers the frequency range of its civil signal (cf. Eq. 1). In order to avoid carrying out this signal processing step with both signals, this filter can be also applied in the cross-spectral domain. An inverse Fourier transformation of this band-pass limited cross-spectrum provides then the relative time-delay between the direct and reflected signal.
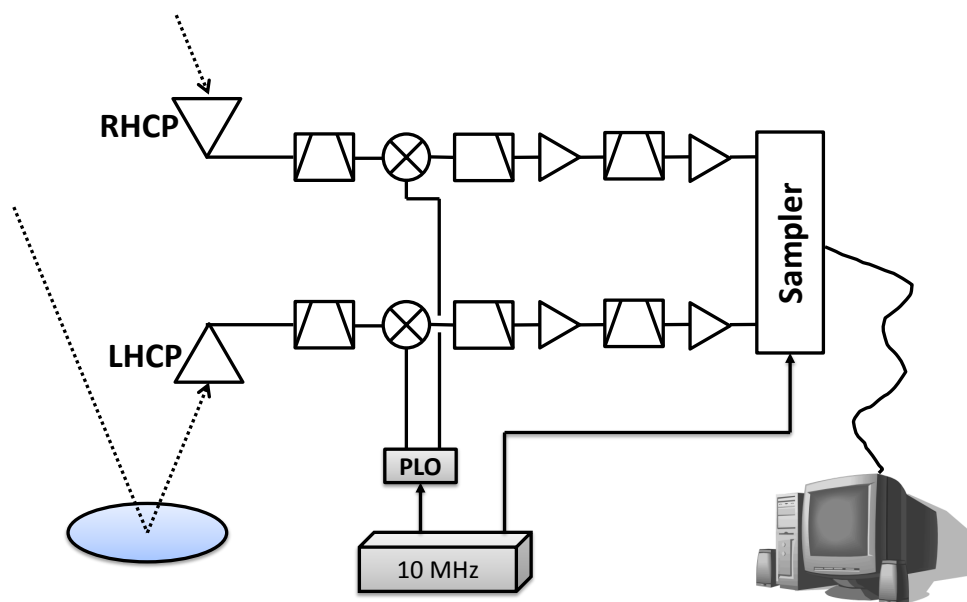
Figure 2. Diagram of the GLONASS-R RF front-end. RHCP and LHCP signals are coherently down-converted to base-band. After A/D conversion, signals are sent via USB to a PC for further processing.
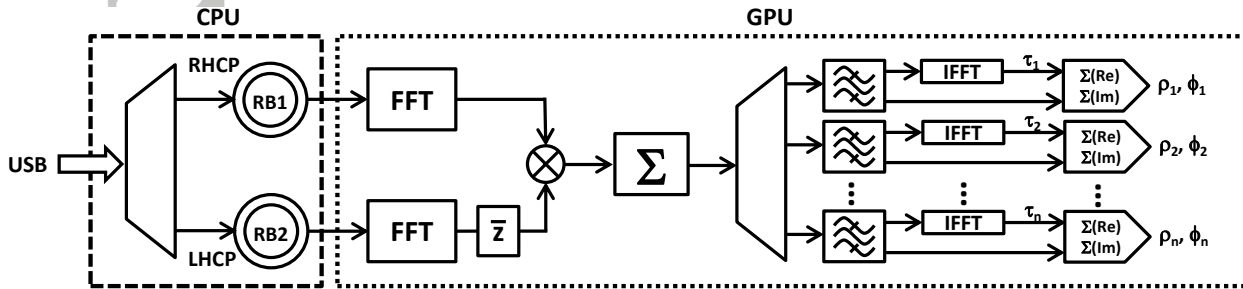
Figure 3. Schematics of the software defined radio which handles all signal processing after data have been sent to the PC via the USB bus. A CPU thread splits the incoming data in RHCP and LHCP signals and stores them in a circular (or "ring") buffer (RB) from where the data are transferred to GPU memory in one second batches. After applying parallel streamed FFT with a length of 1 millisecond on both signals, the cross-spectrum is obtained and coherently integrated to the prior epochs ($\bar{z}$ denotes the conjugate complex operator). Every T seconds, satellites are selected by applying a band-pass that matches with the corresponding GLONASS channel and then inverse Fourier transformed. As results, the delay τ_i, the interferometric phase ϕ_i and the correlation amplitude ρ_i are obtained for each satellite and integration period .
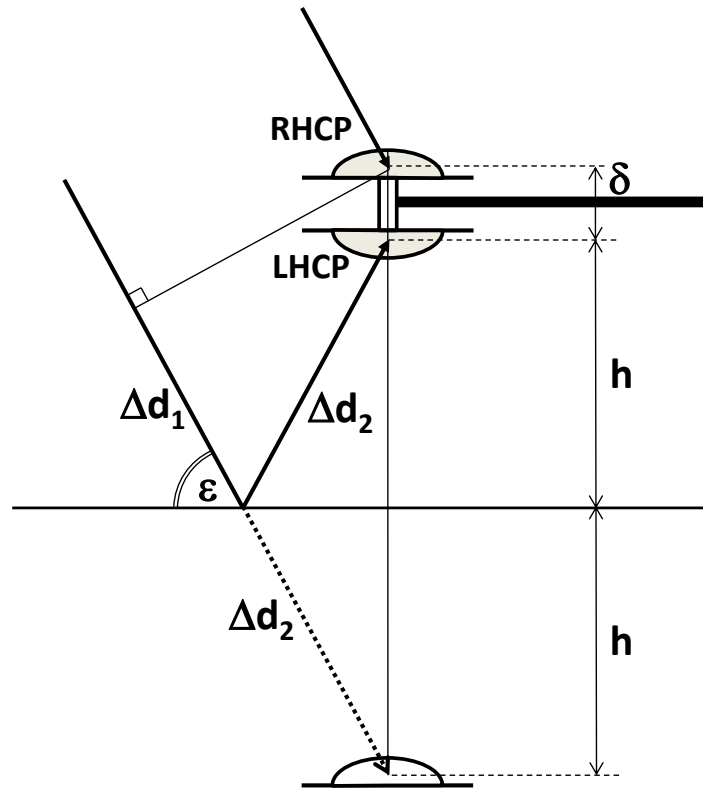
Figure 4. Geometric situation for a GNSS-R system with the RHCP antenna placed vertically above the LHCP antenna. The antenna phase centers are separated by a distance δ, and the LHCP antenna is thought to be located at a vertical distance h above the reflecting surface. Mirroring the LHCP antenna's position on the water surface, i.e. virtually positioning the antenna at a distance h below the water surface, allows to deduce a simple geometric relation between excess path $\Delta d_1 + \Delta d_2$, elevation angle ε and h. The relation $\Delta d_1 + \Delta d_2 = (2h + \delta) \cdot \sin \varepsilon$ is obtained, which is valid as long as the vertical axis, defined by the two antennas, is perpendicular to the reflecting surface.

Figure 5. A photo of the GNSS-R based tide gauge installation at the Onsala Space Observatory, Sweden. Up-(RHCP) and downward (LHCP) looking GNSS antennas are mounted on a beam extending over the sea surface, which makes is possible to collect reflections from the open sea towards the South (cf. Fig. 6).
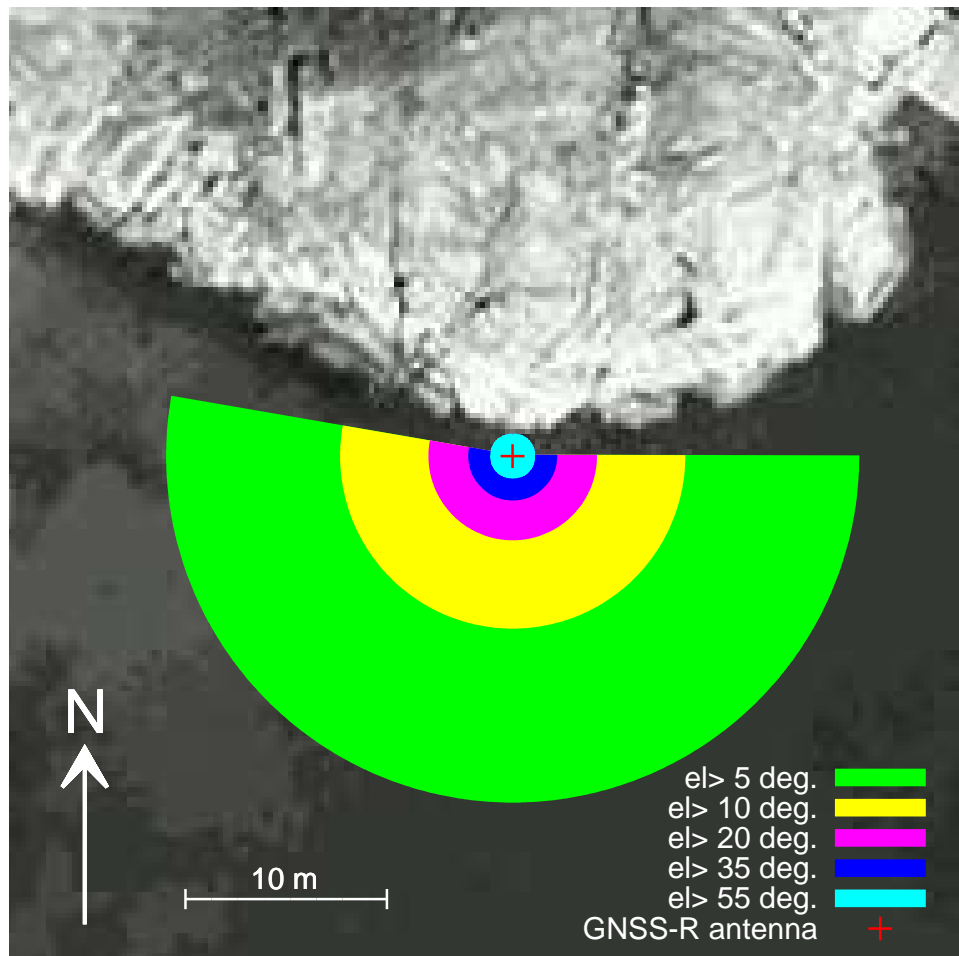
Figure 6. Aerial image of the GNSS-R tide gauge at the Onsala Space Observatory. The location of the GNSS antennas is marked with a red cross, and colored sectors mark the collection area on the sea surface for different elevation cut-off angles. For elevation angles lower than 55° the azimuth range is restricted to values between 90° and 280°. For elevation angles larger than 55° no azimuth restriction applies as both antennas are mounted on a beam which is positioned over the sea water.
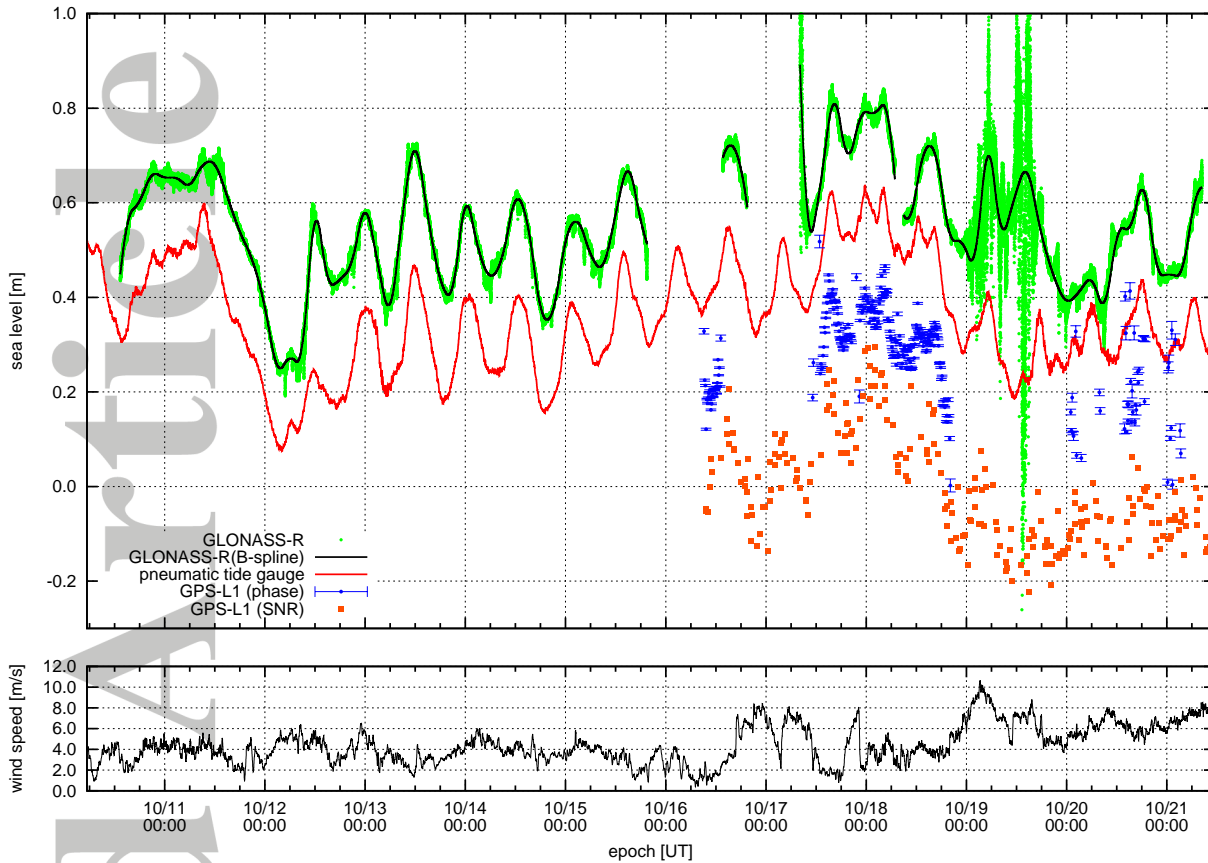
Figure 7. Upper plot: Tide gauge measurements (red line) are plotted together with GLONASS-R results (green dots and black line), GPS L1 GNSS-R estimates (blue dots) and results derived from GPS L1 SNR data (orange squares). The GLONASS-R results are shown as both fitted B-spline models (black line) and high-frequency results based on back-substitution of estimated phase offsets (green dots). Individual mean values have been subtracted from each time series, and to improve the readability of the figure the time series are presented with offsets of 20 cm. Lower plot: Wind speed measurements from the weather station at the Onsala Space Observatory.
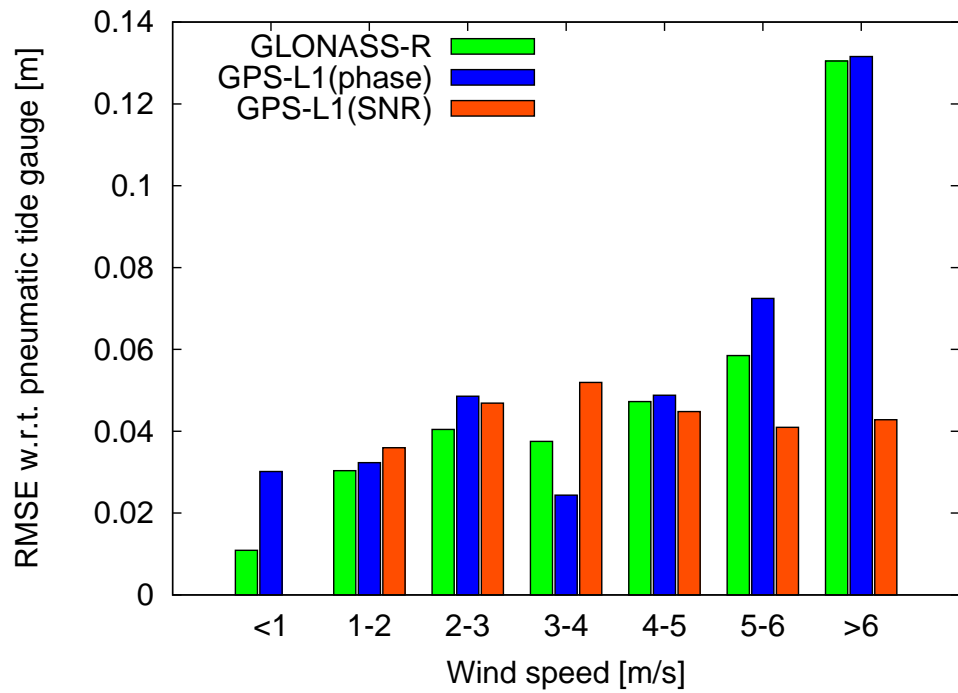
Figure 8. Root-mean-square error (RMSE) of back-substituted GLONASS-R and GNSS-R results w.r.t. the pneumatic tide gauge readings, grouped for different wind speeds.
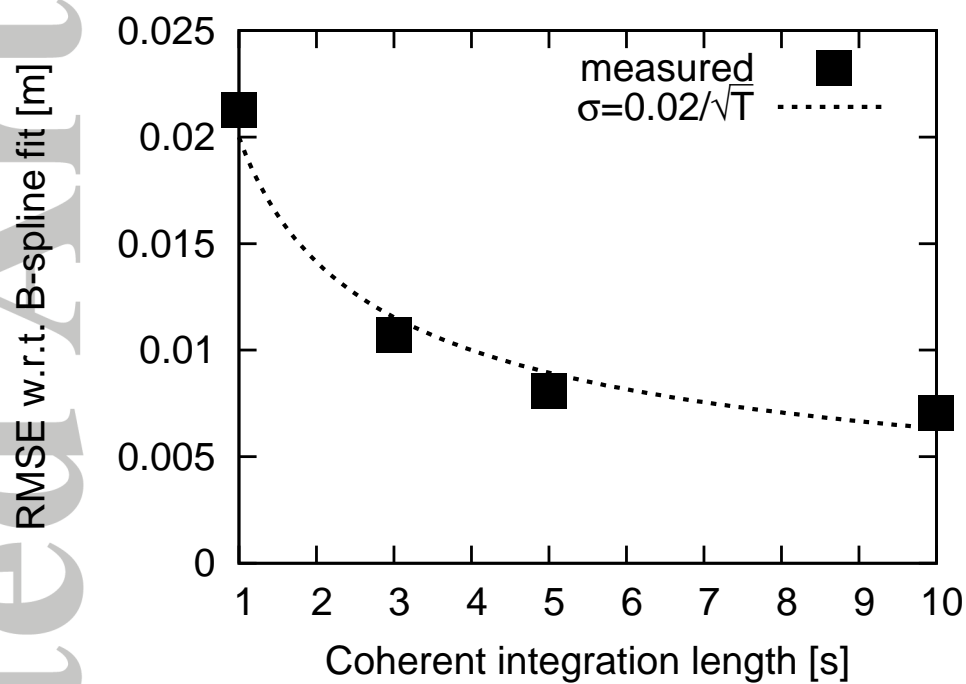
Figure 9. Post-fit root mean square error (RMSE) of the B-spline approach for different values of coherent integration length.